



Femtosecond laser micromachining for stress-based figure correction of thin mirrors

HENG ZUO,* RALF HEILMANN,  AND MARK SCHATTENBURG 

MIT Kavli Institute for Astrophysics and Space Research, 70 Vassar St, Cambridge, Massachusetts 02139, USA

*Corresponding author: zuoh@mit.edu

Received 20 April 2022; revised 29 August 2022; accepted 7 September 2022; published 20 October 2022

The fabrication of a large number of high-resolution thin-shell mirrors for future space telescopes remains challenging, especially for revolutionary mission concepts such as NASA's Lynx X-ray Surveyor. It is generally harder to fabricate thin mirrors to the exact shape than thicker ones, and the coatings deposited onto mirror surfaces to increase the reflectivity typically have high intrinsic stress that deforms the mirrors further. Since the rapid development of femtosecond laser technologies over the last few decades has triggered wide applications in materials processing, we have developed a mirror figure correction and stress compensation method using a femtosecond laser micromachining technique for stress-based surface shaping of thin-shell x-ray optics. We employ a femtosecond laser to selectively remove regions of a stressed film that is grown onto the back surface of the mirror, to modify the stress states of the mirror. In this paper, we present experimental results to create both isotropic and anisotropic stress states on thin flat silicon mirrors with thermal oxide (SiO₂) films using femtosecond lasers. We show that equibiaxial stress can be generated through uniformly micro-machined holes, while non-equibiaxial stress arises from the ablation of equally spaced troughs. We also present results from strength tests to show how this process minimally affects the strength of mirrors. These developments are beneficial to the high-throughput correction of thin-shell mirrors for future space-based x-ray telescopes. © 2022 Optica Publishing Group under the terms of the [Optica Open Access Publishing Agreement](https://doi.org/10.1364/OPTICA.461870)

<https://doi.org/10.1364/OPTICA.461870>

1. INTRODUCTION

Thin silicon optics are considered great candidates for a variety of space missions and are actively being researched for a number of space telescopes, from segmented mirrors for next generation space x-ray telescopes [1] to ultra-lightweight deformable mirrors [2]. For instance, the Lynx X-ray Observatory is a flagship mission concept funded for study in the 2020 NASA Astrophysics Decadal Survey to provide x-ray vision for supermassive black holes, galaxy formation, stellar evolution, etc. [1]. To achieve its science objectives, Lynx requires a large number (~37,400 pieces) of densely packed, grazing-incidence, thin-shell silicon mirrors, each of thickness from 0.5 to 4 mm while maintaining half-arcsecond half-power diameter (HPD) on-axis angular resolution, to make up the telescope assembly with an outer diameter of 3 m and a total effective area greater than 2 m² at 1 keV. It is critical for this mission to have thin accurately figured mirrors with high-reflectivity x-ray coatings to enable the orders-of-magnitude gains in throughput and field-of-view size for sub-arcsecond imaging over previous telescopes.

However, it is quite challenging to obtain thin mirrors to the exact shape with high optical quality, because they tend to deform easily during fabrication. Several different types of mirror materials have been explored for x-ray telescopes in the past few decades, from ceramics and glass to silicon. For example, one technology under development for Lynx by NASA Goddard Space Flight

Center is the Silicon Meta-shell Optics concept [3], which applies advanced polishing technologies to monocrystalline silicon. Due to its low density, low coefficient of thermal expansion, high thermal conductivity, and near-zero internal stress, monocrystalline silicon makes an attractive material choice for space telescope mirrors. Though recent advances in mirror fabrication techniques such as silicon pore optics [4] and monocrystalline silicon polishing [5,6] have made great progress towards accurate production of thin mirrors, telescope mirrors still need to be coated with highly reflective coatings, which typically have nonuniform intrinsic stress that deforms the mirror. Common choices for these reflective coatings include single-layer heavy metal films such as iridium [7–9], and multilayer films [10,11]. Typical single-layer iridium films of 15 nm thickness deposited with magnetron sputtering have low roughness (about 5 Å) and high density, but large intrinsic stress (about –3 GPa, minus sign representing compressive stress) [8], which results in an integrated stress (the film stress integrated over its thickness) of about –45 N/m. This will lead to a large amount of distortion beyond telescope tolerance. Chalifoux *et al.* [12] showed that Lynx may require integrated stress magnitudes of <0.2 N/m and film thickness non-uniformity better than ±1% for each piece of mirror to achieve its required resolution. This is especially difficult to achieve on a curved mirror substrate. Annealing a single-layer film or multilayer films may only reduce but not eliminate the intrinsic stress [7], and may affect the film composition and roughness [13,14], which impacts the reflectivity.

Various techniques have been explored to correct for shape errors during the fabrication process and to reduce distortions from the coating film stress, including surface finishing methods such as ion-beam figuring (IBF) and magnetorheological finishing (MRF), both of which have been widely used in the semiconductor industry for trimming wafer thickness. These deterministic methods can be used to correct surface height errors in mirrors [15], but their low material removal rates make it time consuming and expensive to apply to a large number of thin mirrors for large aperture telescopes, and the significant amount of heat generated during the process is hard to remove from the optics in a vacuum chamber. In addition, these methods can be applied only prior to the deposition of coatings that enhance mirror reflectivity, and thus they cannot correct for the coating distortion of thin mirror substrates.

Another approach is the stress-based figure correction method, which exploits the bendability of thin mirrors and applies stress at or close to the back surfaces of mirror substrates to manipulate them into their desired shapes. A 2D stress field is applied to induce controlled bending by adjusting the planar stress components in the thin mirrors without introducing additional surface height errors. Several passive and active methods have been developed for this purpose. For example, piezoelectric film adjusting is an active *in situ* correction technique that applies patterned piezoelectric films that expand or contract in response to an applied electric field onto thin glass mirror substrates [16]. It is a complex process to design and apply the hundreds of pieces of piezoelectric cells to a single mirror, while the activation of one piezoelectric cell results in an approximate gradient of figure change of about $10''$ [17,18], which is still relatively large for the science goal of many planned missions. Ion implantation [19], on the other hand, is a passive approach that applies a static correction where high-energy ions are implanted into a thin mirror substrate to generate stress near its surface. It requires a large expensive ion generator and operates in vacuum, and it has been shown to correct the substrate shape to within 60 nm RMS, in most cases to within 1/20th of the coating deformation [20]. Another method is oxide patterning with photo-lithography and acid etching, which utilizes a micro-patterned silicon oxide layer on the back side of the substrate. It has been shown to reduce the stress-induced distortions in flat silicon substrates by a factor of 68 for RMS surface height [21]. In spite of the high accuracy, this process includes over 10 time-consuming steps, most of which need to be done inside a clean room.

To take advantage of the stressed film figuring method while avoiding some of the problems, we started to investigate another approach—femtosecond laser micromachining, which combines advanced laser machining technology with the stress-based figure correction technique. The nonlinear nature of the ultrafast laser–matter interaction leads to many unique advantages for femtosecond laser micromachining in target materials over other fabrication techniques, such as with photo-lithography and excimer lasers. Traditional laser processing methods typically use laser sources with pulse widths of nanoseconds or longer, resulting in greater thermal effects including a large heat-affected zone, shock waves, and micro cracks. Molten material at the focus of the laser beam can be ejected to the surface and form a recast layer, leaving a significant amount of debris and causing damage to adjacent structures. In comparison, ultrafast lasers are capable of controllably producing highly precise features, such as holes, channels, and marks on various materials with little collateral damage, as heat

diffusion outside the laser focused area is minimized [22,23]. The three-dimensional degree of freedom of ultrafast micromachining and its material independence [24,25] enables fabrication in compound substrates composing several different materials including single- or multilayer films. In addition, advanced femtosecond lasers have high repetition rates that allow for much higher machining speeds and throughput than many traditional methods, which makes it a promising figuring method for fast high-volume figure correction of the large numbers of ultrathin mirrors required in next-generation space-based x-ray telescopes.

In this paper, we first describe the methodology of applying the stress-based figure correction approach with femtosecond lasers. Then we present experimental results on thin flat silicon mirrors with thermal oxide films to show that non-equibiaxial stress states can be generated through the ablation of equally spaced troughs. Further, we present a series of strength test results to show to what extent this process affects the strength of mirrors.

2. METHODOLOGY

A. Stress-Based Figure Correction Approach

Many substrate deformations are undesirable effects, as in the case of mirror coatings where a thin stressed film is applied to the mirror surface to enhance the reflectivity. With an appropriate film stress field applied to the mirror's backside surface, a desired deformation field can be created and the figure of the mirror can be improved. The stress can be applied through either a distinct stressed film, or to the substrate at or near the surface. The mechanism of deforming a mirror using an additional stress field relies on an internal strain generated in a thin region of a relatively much thicker substrate. Here, we consider the case of a thin stressed film on a substrate. With the thin film laterally constrained by the substrate, an in-plane stress field develops within the film. No external loads or constraints are applied to the substrate, and this film stress bends the substrate until the substrate–film system reaches an equilibrium. By manipulating the stress field in the film applied to the substrate, we can control the deformation field of the substrate–film system, which is chosen to eliminate any undesirable surface figure errors in the mirror.

Mathematically, a general stress tensor has six independent components, while in the plane stress case, only three in-plane stress components contribute significantly to the substrate deformation. The condition for simplification requires that the thin mirror substrates are acted upon only by parallel load forces, and this is satisfied given the film is thin compared to the substrate thickness. Various approaches have been developed for applying film stress to generate a controlled deformation in thin mirrors, and they can be split into two categories based on the type of stress they apply, i.e., equibiaxial stress, or general biaxial stress. Many previous attempts in stressed film figuring methods are focused on applying equibiaxial stress only, which limits the types of mirror distortion that can be accurately corrected. It can be useful to correct the deformation caused by another equibiaxial film stress, such as from a deposited reflective film, in which case the equibiaxial stress field alone will be sufficient. However, for many other types of mirror distortions, general biaxial stress fields are needed to achieve exact figure correction of arbitrary surface figure errors in thin mirror substrates [26]. This requires applying a non-equibiaxial stress state, which includes both antibiaxial stress and shear stress, in addition to equibiaxial stress.

The challenge in applying general biaxial stress is that it requires controlling three variables, whereas for equibiaxial stress, only one variable is controlled. There are fewer approaches to applying non-equibiaxial film stress that have been developed than those for equibiaxial stress. Patterning a stressed film, for example, by writing lines with width comparable to the film thickness can result in a non-equibiaxial stress state [27]. By carefully choosing the rotation angle and aspect ratio of the lines, a non-equibiaxial field can be generated with the stressed film, as has been shown both theoretically [28] and experimentally [29]. A practical challenge with this approach is to pattern large surface areas with very small non-repeating features. Additionally, the micro-fabrication tools built for the semiconductor industry, such as photo-lithography, are designed to work on flat wafers but not curved mirror substrates that are of interest to x-ray astronomy.

Building upon these existing methods, we have developed two different types of approaches to correct for equibiaxial and general biaxial stress components, with advantages distinct to ultrafast laser micromachining techniques.

Method I. Ultrafast laser micro-stressing, focused on the “introduction of stress” to mirrors, relies on internal modification of glass mirrors. Laser pulses are focused inside the back surface of a mirror substrate, creating locally stressed volumes in the focal regions, which then leads to substrate bending and further deformation. This work has been demonstrated on fused silica glass, and equibiaxial stress states have been generated [30]. An example of the micromachining parameters used in that work were individual laser spot size $\sim 2 \mu\text{m}$, pulse energy $\sim 50 \mu\text{J}$, and micromachining depth $\sim 50 \mu\text{m}$ [30].

Method II. Stressed film patterning with ultrafast lasers, focused on the “removal of stress” to silicon mirrors with stressed films, is a modification to the method of patterned removal of a stressed film. Femtosecond laser surface ablation is applied to correct for thin mirrors with patterned stress fields, through the selective removal of stressed film regions and adjacent substrate regions. It is capable of applying both equibiaxial stress and non-equibiaxial stress components. This is the focus of this paper, and the design and experimental setup are the subject of the next section. A wide range of micromachining parameters can be used in this method. For example, in this work, we used a femtosecond laser with spot size of $\sim 2 \mu\text{m}$, pulse energy from 0.1 to 20 μJ , and depth of removed region from 0.5 to 20 μm .

Both methods can be applied to curved mirrors with a different setup to allow for three-dimensional movement of the substrates. The two methods are illustrated in Fig. 1.

B. Process Flow

A series of preparation steps is needed to apply a stressed film to a mirror substrate to correct figure errors caused by fabrication errors or coating distortions. A thin film of stressed material is first applied onto the substrate back surface, which is then selectively ablated with femtosecond lasers. By removing portions of the stressed film at different substrate locations in a controlled fashion, the imparted film stress is partially relieved. The stressed film we use here is the thermal oxide of silicon (SiO_2). Research has shown the growth of thermal oxides on silicon to be repeatable and the resulting films to be stable, and the films have an intrinsic compressive stress of in the range of 300–450 MPa, depending on a number

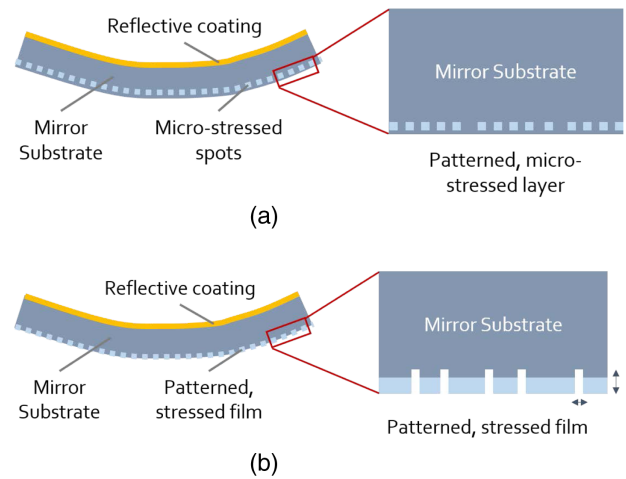


Fig. 1. Illustration of the two stressed film figuring methods for correcting thin mirrors using ultrafast lasers. (a) Method I: ultrafast laser micro-stressing. Laser pulses are focused inside the back surface of a mirror substrate, creating locally stressed volumes in the focal regions, which then leads to substrate bending and further deformation. (b) Method II: stressed film patterning with ultrafast lasers. Femtosecond laser surface ablation is applied to correct thin mirrors with patterned stress fields, through the selective removal of stressed film regions and adjacent substrate regions.

of factors such as the growth temperature and substrate orientation [31,32].

Starting with a bare silicon mirror with figure errors to be measured and corrected, a thin layer of silicon dioxide (SiO_2) needs to be applied to both sides of the silicon mirror substrate. The oxidation can be done by exposing the mirror substrate to a combination of oxidizing agents and heat to grow thermal oxides on its surfaces. The integrated stress of the oxide film can be adjusted by varying the thickness in the oxidation step, such as controlling the oxidation time. Then, the oxide film on the front side of the mirror is removed with buffered oxide etch, while the backside oxide is protected by a layer of photoresist, which is removed later with piranha solution. The surface profile of the mirror substrate is measured before and after this step of oxide removal, to determine the effective stress map of the thermal oxide at the back surface of the substrate. Then, the mirror front side is coated with a highly reflective film coating, and some thermal annealing cycles might be needed to ensure the stability of the coating. After that, the surface profile of the mirror’s front side is measured again and compared to the target shape to generate an error map for correction. Up to this point, the process is similar to the process for thermal oxide patterning with photo-lithography [21], but the difference is in the following step.

Next, as shown in Fig. 1(b), laser pulses are focused onto the thermal oxide film on the back side of the mirror substrate to create a series of features such as holes or troughs. The dimensions of these features are on the order of 10 μm . The removal of the stressed film inside these features allows the material in the adjacent regions to relax. The removal of the stressed film and the relaxation of adjacent substrate regions together contribute to further stress relaxation and substrate bending. To achieve this stress relief over the full mirror, the substrate is moved perpendicularly to the laser beam to expose various regions across the whole substrate. A stress field that corrects the error map is calculated, and a removal pattern is derived that determines the amount of material to be removed in

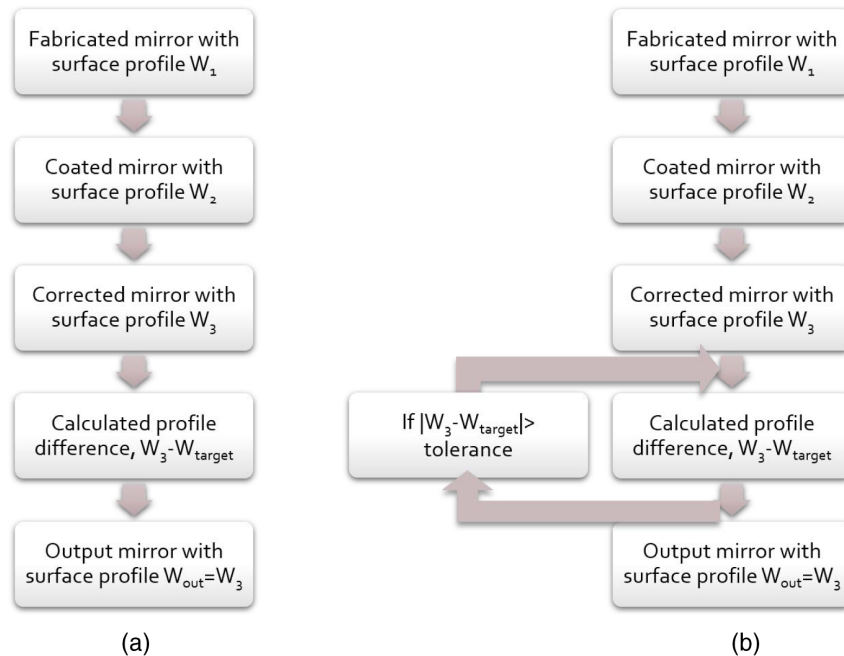


Fig. 2. Illustration of single- and multi-pass correction schemes. Most stressed film figuring methods are capable of applying only one correction pass, even if the target mirror profile has not been reached. In comparison, using ultrafast laser micromachining can enable a multi-pass correction scheme, where a feedback loop is implemented to reduce the figure error terms repeatedly until an acceptable mirror profile has been achieved. (a) Single-pass correction scheme. (b) Multi-pass correction scheme with a feedback loop.

different regions, as discussed earlier. By tuning the micromachining parameters in different regions, the figure errors in the coated silicon mirror can be removed. After the correction step, the mirror surface profile is measured again and compared to the target surface profile.

In addition, we introduce a multi-pass correction scheme that can greatly improve the results. Figure 2 shows two types of correction schemes for implementing stressed film figuring methods. Most stress-based figure correction methods are capable of applying only one correction pass as shown in Fig. 2(a), even if the target mirror profile has not been reached. The process flows from top to bottom, starting with a fabricated mirror that has some figure errors to be corrected, since most fabrication processes are not perfect. The surface profile of the front side of the mirror is marked as W_1 , which is measured with a metrology tool, such as an interferometer or a Shack–Hartmann tool. Then, the mirror is coated with highly reflective film coatings such as iridium, and some thermal annealing cycles may be needed to ensure the stability of the coating over time. After that, the mirror's front side is measured again with the same metrology tool to obtain a surface profile, marked as W_2 . It is then compared to W_1 to determine the mirror distortion from the coating stresses. It may also be compared directly to the target mirror profile W_{target} to determine the total figure error map from both the fabrication process and coating distortion. After obtaining the error map, the stressed film figuring method will be used to correct for it. A map of the stress field that will be applied to correct for the error map can be calculated in a number of ways, such as those described by Chalifoux *et al.* [26]. The mirror is then measured on the front side again to obtain its final surface figure, marked as W_3 . This process basically ends here, regardless of the difference between the obtained mirror profile and the target mirror profile $\|W_3 - W_{\text{target}}\|$.

In comparison, with multi-pass correction, a feedback loop is implemented to reduce the figure error terms repeatedly until an acceptable mirror profile has been achieved, as shown in Fig. 2(b). After the last step of obtaining a surface measurement W_3 , it is compared with the target mirror profile W_{target} to generate a difference map $W_3 - W_{\text{target}}$. If the absolute difference is greater than the acceptable tolerance, then the mirror needs to go through the correction process again, and a new map of the stress field that is needed to correct for the new error map will be calculated and applied. This correction-measurement-comparison step can be repeated multiple times until the calculated difference between the obtained mirror profile and the target profile is smaller than the tolerance. One should be careful, though, not to over-correct the figure errors in one pass, because it would be difficult (though not impossible) to reverse the process. (This will be discussed in another paper in preparation.) In practice, a good approach is to ensure that a thick enough stressed film is deposited on the back side of the mirror, such that only one type of stress (tensile or compressive) needs to be applied to compensate for coating distortions. In addition, it would be beneficial to always leave some margin in one correction pass so that it is more forgiving to mistakes.

This multi-pass correction scheme may not seem a significant innovation from the single-pass correction scheme, but in practice, it is difficult for many other types of stressed film figuring methods to perform more than one correction pass. For example, with the photo-lithography and etching method, over 10 steps of time-consuming clean-room processes are needed to etch the micrometer-scale features inside the thermal oxide film. If a mistake is made, or if the designed pattern of the stress map fails to correct all the terms in the error map, which is likely to happen, it is difficult to reverse back and create another lithography pattern and etch into the processed surface. This problem, however, can be solved with ultrafast laser micromachining, where the ultrafast

laser beam can be used as a fine stress correction method, on top of the first coarse correction pass done by photo-lithography, for example, to trim off any additional oxide and correct for residual error terms. It is also more forgiving with process control excursions for each correction pass and enables the combination of different stressed film figuring methods. This technique can also be used in conjunction with other stress-based figure correction techniques, to target different spatial-frequency errors.

C. Stress Analysis and Stress Field Calculation

Two other issues to be addressed in the application of stressed film figuring methods are: how to calculate the stress field from the surface measurements, and how to derive a stress map to achieve the needed deformation field. As mentioned above, the mirror surface profile needs to be measured multiple times during the correction process, which we do with either an interferometer or a Shack–Hartmann metrology tool. The difference between two measurements represents the change in the surface profile caused by the intervening process, and this difference map of the substrate surface can be reconstructed by fitting to a set of basis functions. These could be Legendre polynomials for rectangular substrates such as the Lynx flight mirrors, or Zernike polynomials, in the case of circular wafers used for laboratory testing to reduce costs.

The deformation of the thin-film/substrate system is proportional to the stress in the film integrated over its thickness, i.e., the integrated stress, which is equivalent to the mean film stress multiplied by the film thickness. For a uniform integrated stress field, the change of curvature of the substrate can be calculated from Stoney's equation [33] for an equibiaxial stress state, or Stoney's equations by Suresh and Freund [27] for a general biaxial stress state. The relationships between the substrate curvature and the integrated film stress $S_{\alpha\beta}$ (α, β taken from x, y) are as follows:

$$S_{xx} = \frac{E_s h_s^2}{6(1 - \nu_s^2)} (\kappa_{xx} + \nu_s \kappa_{yy}), \quad (1)$$

$$S_{yy} = \frac{E_s h_s^2}{6(1 - \nu_s^2)} (\nu_s \kappa_{xx} + \kappa_{yy}), \quad (2)$$

$$S_{xy} = \frac{E_s h_s^2}{6(1 - \nu_s^2)} \kappa_{xy}, \quad (3)$$

where E_s and ν_s are the Young's modulus and Poisson's ratio of the substrate, and h_s and h_f are the thickness of the substrate and film, respectively; $h_f \ll h_s$. κ_{xx} , κ_{yy} , κ_{xy} are the curvatures of the film/substrate system, where the former two terms are the curvature in x and y directions, and the last one represents a twist of the substrate's midplane. The mean stress of the film can then be derived by dividing the integrated stress by the thickness of the film:

$$\sigma_{xx} = \frac{S_{xx}}{h_f}, \quad \sigma_{yy} = \frac{S_{yy}}{h_f}, \quad \sigma_{xy} = \frac{S_{xy}}{h_f}. \quad (4)$$

The above formula provides a stress map of the thin mirror from measurements of its surface profiles.

Much work has been published on creating non-uniform, equibiaxial stress fields to generate a desired displacement field, focused mostly on flat plates [34,35]. Several authors have presented mathematical formulas [36] and analytical solutions [26] to create general biaxial stress fields on a round flat plate. Chalifoux

et al. [26] has shown two general biaxial stress fields that can correct any figure error field in thin flat plates. One of them is trivial, and is essentially the inverse of Stoney's equations [Eqs. (1)–(3)]. The other one provides a numerical displacement field as linear combinations of Zernike polynomials. In addition, they show that equibiaxial stress, though easy to generate, can be used to make only approximate corrections, while all three plane stress components are needed to achieve exact figure corrections for general error fields.

After a stress field is obtained to achieve the needed deformation to correct for the figure errors and/or compensation of undesired stress from coatings in a mirror substrate, it needs to be translated into a pattern that can be applied to the mirror substrate with the corresponding correction method. This pattern is essentially a combination of an equibiaxial field and a non-equibiaxial field, for each individual point on the mirror surface. It should be noted that there is a shear stress component σ_s^f (superscript f represents "film") in the original plane stress decomposition, and it is not easy to physically apply in the methods that we have developed. However, it can be worked around, by performing a transformation of axes and rotating the stress field at an angle of θ , such that the shear component vanishes in the transformed coordinates. This is essentially equal to finding the principal planes for each point on the mirror surface. The angle of transformation is given by $\tan 2\theta = \frac{2\sigma_{xy}^f}{\sigma_{xx}^f - \sigma_{yy}^f}$, and new equibiaxial and antibiaxial components in the transformed coordinates are

$\sigma_e = \sigma_{xx}^f + \sigma_{yy}^f$, $\sigma_a = \sqrt{(\sigma_{xx}^f - \sigma_{yy}^f)^2 + 4\sigma_{xy}^f{}^2}$ (subscripts e and a represent "equibiaxial" and "antibiaxial," correspondingly). After identifying the orientation angle for each individual point on the mirror surface, we are left with the task of applying the two stress components σ_e , σ_a with our chosen stressed film figuring method. There are also other more involved patterned structures that could better spatially manipulate the three plane stress components [37].

Our method relies on having a library of polynomials that represents different figure error terms and is correctable with equibiaxial and non-equibiaxial stress components. In the next section, we will describe ways to generate these two stress fields in thin mirror plates.

3. EXPERIMENTS

We primarily demonstrate applying this method on flat silicon wafers in the experiments. The "flat plate model" is the limiting case of a thin-shell mirror substrate when its radius of curvature R approaches infinity, and it is an important preliminary step towards correcting curved mirror segments. The error that needs to be corrected for a mirror should not have surface height errors larger than tens of micrometers. In this case, after subtracting the ideal (or target) figure from the measured figure of the mirror surface profile, the difference map can be described with a flat plate model well enough. Though the analysis in this paper is constrained to flat mirror substrates, it in principle applies to the difference map of curved mirror substrates as well.

A. Experiment Setup

We designed an optics system to micromachine flat silicon wafers. The first version of the system was equipped with an IR femtosecond laser beam from IPG Photonics, and the results were

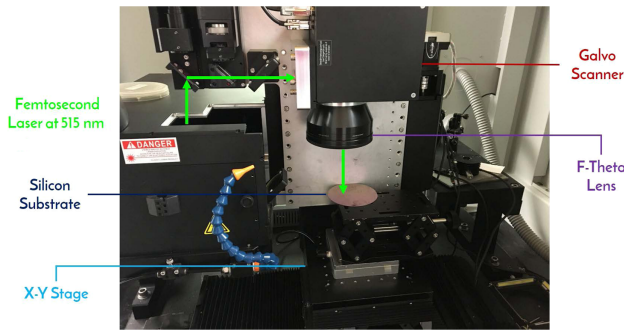


Fig. 3. Laser micromachining system setup at Advanced Optowave Corporation. The femtosecond laser delivers a pulse width of $\tau = 800$ fs at a pulse frequency of 100 kHz. The wavelength is $\lambda = 515$ nm after second harmonic generation.

previously presented [38]. The second version uses a green femtosecond laser (AOFemto series diode-pumped solid-state laser) from Advanced Optowave Corporation (Ronkonkoma, NY). It has a pulse width of $\tau = 800$ fs at a pulse frequency of 100 kHz. The wavelength is $\lambda = 515$ nm after second harmonic generation. The waist of the Gaussian beam at the focus on the substrate is about $2 \mu\text{m}$. The system setup is shown in Fig. 3.

The green arrows illustrate the light path of the femtosecond laser beam from the box where it is collimated before it reaches the sample. The red line points to a galvo scanner head, which contains two galvanometer scan mirrors (one for each axis) to direct the laser beam to any position in the horizontal plane in the field of view ($30 \text{ mm} \times 30 \text{ mm}$). It allows for very fast scanning speed—up to 3000 mm/s , and provides flexibility for arbitrary scan patterns not limited to just dots or straight lines. The purple line points to an F-theta lens, which is designed with a barrel distortion that yields a beam displacement linear with the deflection angle θ , resulting in a planar imaging field. (The beam displacement on the imaging plane is the product of the effective focal length f and θ). With the galvo scanner and F-theta lens, the incoming laser beam can be focused to the same focal plane perpendicular to the optical axis without moving the substrate. The silicon substrate is mounted on top of a fast moving $x - y$ stage. Since the substrate diameter

is 100 mm , larger than the field of the view of the galvo scanner, “stitching” of different fields is needed to cover the whole substrate. In practice, the scanning pattern over the whole substrate was manually divided into 12 sections; within each, the galvo scanner was used to perform a fast micromachining scan. The substrate was then moved to expose a different section using the stage to perform the stitching process, and the stitching precision for this specific system was around $20 \mu\text{m}$.

B. Pattern Design

Knowing how much stress can be created from a uniform micromachining pattern is the stepping stone for further development of stress-based mirror correction. To do this, we need to characterize the amount of stress that can be generated with this micromachining process as a function of various micromachining parameters, such as pulse energy, density of micromachined features, number of laser shots at a single location, etc. Since the stress effects of an individual laser ablated spot is almost immeasurable by the metrology tool, we instead calibrate this effect by applying a uniform micromachining pattern across the whole substrate and then measuring the change of curvature over the substrate surface. A simple way to achieve this is to create equally spaced features, i.e., uniformly distributed holes or periodic troughs. Figure 4 illustrates these two patterns.

Figure 4(a) shows uniformly ablated holes separated by the same distance in both x and y directions. The basic machining pass is a raster scan over a square region ($100 \text{ mm} \times 100 \text{ mm}$), covering the entire 100 mm wafer. The stage carrying the substrate moves in the horizontal plane at a constant velocity. After a fixed machining interval Δ (for example, $\Delta = 500 \mu\text{m}$), the stage pauses and dwells at the same position for a fixed time t_{dwell} (for example, $t_{\text{dwell}} = 50 \text{ ms}$), so that the laser beam can shoot $n_{\text{pulse}} (= t_{\text{dwell}} \times 1 \text{ kHz} = 50)$ consecutive laser shots into the same spot to drill a deep hole. Research has shown that multiple-pulse irradiation alters the substrate materials more readily than single-pulse irradiation [39]. In the enlarged picture on the right, the round dark gray dots connected by dotted lines represent a single correction pass in this raster-dwell-scan format. This trace of

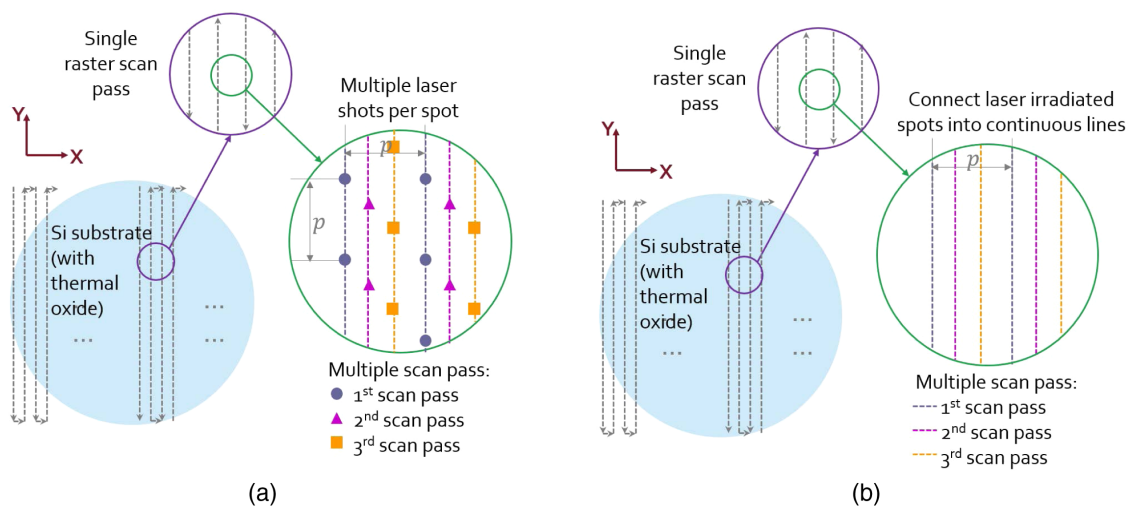


Fig. 4. Two basic machining patterns to characterize the amount of stress that can be generated with various micromachining parameters. (a) Top view illustration of a “uniformly distributed hole pattern” with multi-pass correction using method II (stressed film patterning with ultrafast lasers). Three machining passes are shown in this figure. (b) Top view illustration of a “periodic trough pattern” with multi-pass correction using method II (stressed film patterning with ultrafast lasers). Three machining passes are shown in this figure.

motion is represented by gray dashed lines connecting the round gray dots in the figure. This is referred to as “micromachined holes of multiple exposure,” as each ablated hole in this pattern is exposed to multiple laser pulses. Both Δ and n_{pulse} can be adjusted through the control program.

There are two other types of patterns used, i.e., “micromachined holes of single exposure,” and “micromachined troughs.” As the name indicates, the former is composed of micromachined holes exposed to laser irradiation only once per spot, and the latter involves connecting all the laser irradiated regions into continuous lines. Both can be tested following almost the same process as the one described earlier, and they can all be useful in the correction of an actual mirror with varying shape errors in different regions of the surface. Figure 4(b) illustrates the pattern with periodic ablated troughs parallel to each other. Similarly, a raster scan program is used to run the stage. But instead of the move-and-dwell process along the scan path, the stage moves constantly at a much slower speed (for example, 3 mm/s), such that the laser irradiated regions from different pulses are overlapping on the substrate and every spot along the path is irradiated by multiple laser pulses. The size of the micromachined features we used in these experiments can be found in the next section.

The mirror substrate profiles are measured with a Zygo interferometer before and after each micromachining pass. The change in the surface profile is used to reconstruct a surface height change map by fitting to Zernike polynomials, and to calculate the stress distribution across the substrate caused by the micromachining process. To demonstrate the capability of multi-pass corrections, after measuring the surface profile of the substrate from one micromachining scan pass, we put the substrate back on the stage and micromachine it again, with the same machining pass but offset by a small distance from the first scanning pass. Then we measure the surface profile again and calculate the profile changes to calculate the difference in the stress map. We can add more machining passes as long as there is still enough unmachined film on the substrate. Figure 4(a) shows three different machining passes, where the magenta triangles and the orange squares represent the second and third micromachining passes, respectively. Therefore, the total material removed from the stressed film increases proportionally with the number of total machining passes.

4. RESULTS AND ANALYSIS

In this section, we present experimental results from stressed film patterning through femtosecond laser surface ablation on thin silicon mirror substrates with thermal oxide films. A variety of thermal oxide film thicknesses have been used in the experiments to adjust the maximum magnitude of the integrated stress field

that can be applied to the mirror substrates. The samples used in these experiments are flat silicon wafers of 100 mm in diameter and 525 ± 15 μm in thickness. All of them are coated with a thin layer of thermal oxide on the back side, and some have double-side thermal oxide. The oxides on the front surface do not matter for the experiments described in this paper, as these tests are primarily focused on calibrating the ultrafast laser-induced effects in the mirror substrates as well as for studying the contributing factors in the micromachining process. Therefore, we do not need to have the front surface coated in these experiments. But to carry out the tests for flight mirrors, the mirrors' front sides will need to be coated to enhance x-ray reflectivity. A number of different thermal oxide thicknesses were tested, ranging from 50 to 1400 nm. The experiments are intended to demonstrate that femtosecond laser surface ablation with stressed film patterning can effectively change the surface figure by introducing controlled bending in thin silicon mirrors, hence having the potential to correct for their figure errors as well as compensating for coating distortions.

A. Inspection of Laser Micromachined Features

Preliminary tests were conducted first to map out the parametric space with the laser system. We first inspected the micromachined features using various tools, including a microscope, interferometer, and scanning electron microscope (SEM). Here, we show mainly results from optical microscopes and SEM.

We first examined various features micromachined with the green fs laser system ($\lambda = 515$ nm, $\tau = 800$ fs) under a confocal microscope. By capturing multiple two-dimensional images at different depths, we can reconstruct the three-dimensional structure within the substrate. The sample under test has a 0.5- μm -thick thermal oxide layer on the test surface. Figure 5 shows the images of four micromachined holes exposed to 100 consecutive laser pulses, but with different pulse energies. When the input pulse energy is reduced from 20 to 0.1 μJ , the diameter of the ablated hole drops by only 50% from 14 to 7 μm , while the depth of the hole decreases $30\times$ from 15 to 0.5 μm .

Figure 6 shows images for three micromachined troughs with the same pulse energy (1 μJ) but different deposited energies. The deposited energy is the total amount of energy deposited onto a unit area, and it can be adjusted by changing the scanning speed. The amount of energy deposited per unit area is inversely proportional to the scanning speed. In Fig. 6(a), the scanning speed is 100 mm/s, which is $5\times$ slower than that of Fig. 6(c), so the deposited energy is $5\times$ more. The width of the ablated trough drops by only 12% from 17 to 15 μm , while the depth of the trough decreases by more than half from 0.55 to 0.25 μm .

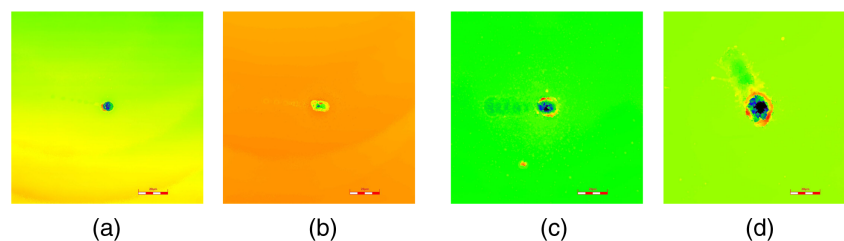


Fig. 5. Confocal microscope images of four micromachined holes exposed to 100 consecutive laser pulses at different pulse energies. (a) Input: pulse energy = 0.1 μJ . Output: hole diameter = 7 μm , depth = 0.5 μm . (b) Input: pulse energy = 0.2 μJ . Output: hole diameter = 11 μm , depth ≥ 2 μm . (c) Input: pulse energy = 2 μJ . Output: hole diameter = 12 μm , depth ≥ 7 μm . (d) Input: pulse energy = 20 μJ . Output: hole diameter = 14 μm , depth ≥ 15 μm .

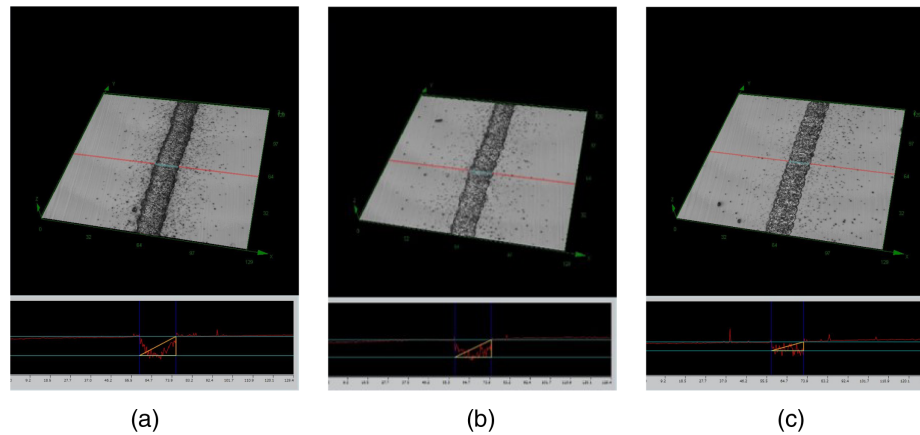


Fig. 6. Confocal microscope images of three micromachined troughs with the same pulse energy ($1 \mu\text{J}$) but different deposited energy. (a) Input: scanning speed = 100 mm/s. Output: trough width = $17 \mu\text{m}$, depth = $0.55 \mu\text{m}$. (b) Input: scanning speed = 200 mm/s. Output: trough width = $16.5 \mu\text{m}$, depth = $0.45 \mu\text{m}$. (c) Input: scanning speed = 500 mm/s. Output: trough width = $15 \mu\text{m}$, depth = $0.25 \mu\text{m}$.

All these modes can be quite useful in actual correction applications, and they can be used in different areas on the substrate to generate desired stress states.

B. Substrate Bending and Integrated Stress Fields

Just knowing the geometry of these micromachined holes or troughs is not enough. We need to know how much stress changes these features can create. A large number of experiments have been done to establish the effectiveness of the method. Part of the results for the uniformly distributed hole pattern has been presented previously [38], and we have demonstrated that this pattern leads to an equibiaxial stress state, as the two stress components in orthogonal directions are very close to each other in magnitude. When applied to the back surface of the mirror, bending moments can be created to impart concave deformations at the front surface, and the curvature of the deformation gets larger as more thermal oxide is removed.

Here, we present surface ablation tests for six samples with thermal oxide patterning using periodic trough patterns. The samples, numbered from 1 to 6, are silicon substrates with 500-nm-thick single-side thermal oxide processed with single-pass micromachining. The trough period is $200 \mu\text{m}$ for all six samples, but they have different trough geometries (width and depth) since they were machined with different parameters. Their shape changes, i.e., the differences of the surface profiles before and after micromachining, are plotted in Fig. 7. The “trough aspect ratio”—a dimensionless parameter defined as the trough depth divided by its width, is measured after micromachining for each sample and also provided in the title. In general, we can see that the substrate bending has different magnitudes in the two orthogonal directions (note that the troughs are parallel to the y direction). This difference of bending moments becomes more prominent as the trough aspect ratio increases, along with larger substrate deformation.

From the measured surface profile changes shown in Fig. 7, we calculated the curvatures and derived the integrated stress field of each sample. The results are shown in Fig. 8, where the vertical axis shows the integrated stress in the two axial directions, and the horizontal axis is the trough aspect ratio. It is clear from this figure that the result is non-equibiaxial tensile stress fields generated in these samples. Laser ablation of troughs in the stressed film creates different bending moments for the mirror substrates in two

directions perpendicular (x direction) and parallel (y direction) to the troughs. A higher tensile stress field is measured in the x direction, as more original compressive film stress is relieved in this direction. We also found that at small trough depths (within a few μm), the laser-induced stress relief effect forms a quasi-linear relationship with the trough aspect ratio. This relationship, however, does not hold when the trough becomes deep (as when the depth becomes comparable to the trough width). We discuss in detail this topic as well as the stress relief mechanism itself in a separate paper [40]. There is also some uncertainty in the measurements, that comes mainly from variations in trough geometry and curvature measurements of the relatively small substrate deformation.

It is also worth noticing that the magnitudes of the laser-induced slope changes and integrated stress fields are quite small, especially in the substrate with 50-nm-thick thermal oxide, where the smallest integrated stress field is $<2 \text{ N/m}$ [41]. This is good because to meet the PSF requirements, the coating stress field still needs to be highly uniform, and the tolerance for non-uniformity in the applied stress field needs to be as small as possible. So, the capability to generate a very small integrated stress field in a controlled manner makes this method promising for applications in x-ray telescope mirrors.

5. STRENGTH TESTS

A concern for the correction method that we are developing is that the small holes and troughs on the surface of the mirror substrates could weaken the mirrors and limit their use for a telescope application. Thus, it is crucial to conduct a series of strength tests to both unmachined and micromachined silicon samples and compare their strength.

There are established test procedures for evaluating the reliability and strength of materials. If any mirrors that are either fabricated or corrected with any of the methods we have touched upon in this paper are intended to be launched into space, then they must show adequate strength to survive launch and harsh space environments. However, the strength of mirrors in many of the proposed mirror fabrication and correction methods has not yet been measured. In this section, we describe our efforts in using a standard ring-on-ring test approach to measure and analyze the breaking strengths of mirror materials.

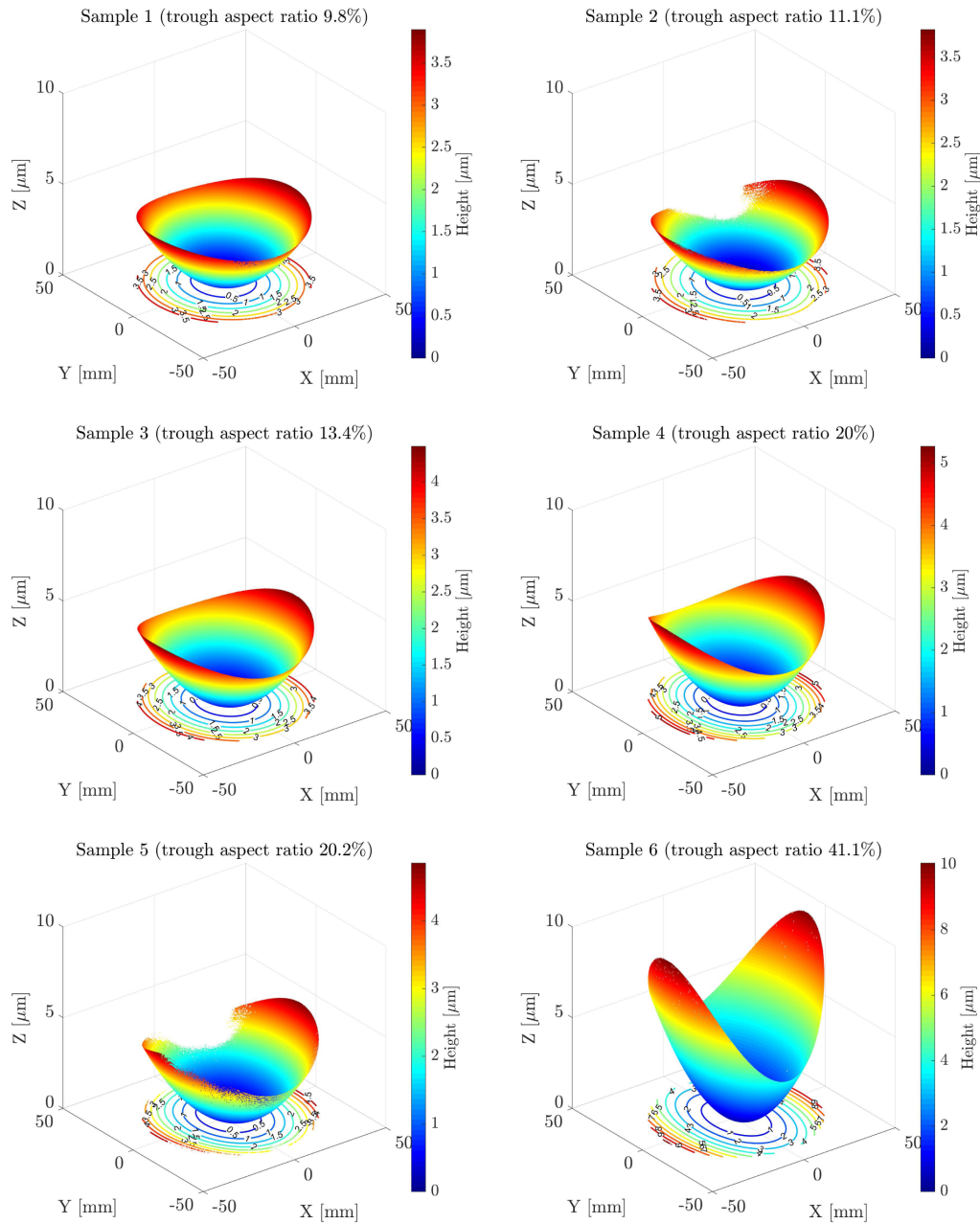


Fig. 7. Measured surface profile changes of six silicon substrates with 500-nm-thick single-side thermal oxide before and after micromachining using periodic trough patterns. The trough period is 200 μm for all six samples, while the measured “trough aspect ratio” is different for each sample, as listed in the title of each figure.

A. Ring-on-Ring Test Setup

Following the standard ASTM C1499, a monotonic load is applied to the specimen, which is supported by a circular ring fixture from the bottom, while the load is applied by a smaller, concentric ring fixture from the top. The sample loading apparatus and setup are shown in Fig. 9. The monotonic loading is applied through an Instron testing machine at the MIT DMSE Laboratory for Physical Metallurgy. The machine can apply loading at a constant rate in a continuous fashion, with no reversals from test initiation to final fracture. A pair of sample holders was built to support the specimen between two load cells in the Instron machine. The load ring (8 mm diameter) applies force to the specimen supported by the support ring (16 mm diameter). Both rings are machined out

of stainless steel to withstand testing samples of high strength. For small deformations of the sample, the loading results in a relatively uniform equibiaxial stress in the region of the sample inside the load ring. The coupling ball between the load cell and the load ring plate uniformly distributes the loading on the specimen.

The specimens are hand cut ~ 30 mm square from a silicon wafer. Each wafer can provide up to seven specimens. Teflon tape is used on the compressive surface of the specimen to minimize friction. To start the test, the specimen is placed on the center of the support ring plate on a load cell, and the load ring plate is aligned to the bottom plate. The coupling ball is placed in a divot on top of the load ring plate, and the load cell is lowered slowly until it is almost touching the ball. The Instron machine is set to apply

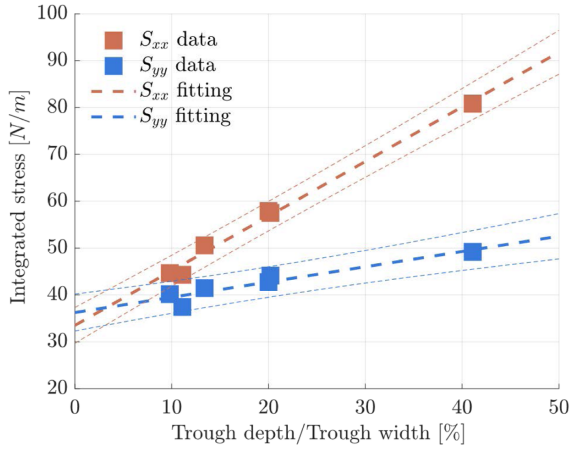


Fig. 8. Laser-induced integrated stress fields in six silicon samples of 500-nm-thick single-side thermal oxide, machined with periodic trough patterns. The trough period is 200 μm for all six samples, but they have different trough geometries (width and depth) since they were machined with different parameters. Non-equibiaxial stress fields are generated in this series of tests.



Fig. 9. Photographs of silicon wafer strength testing setup with an Instron machine using ring-on-ring test. Left: Instron machine used to apply the monotonic loading. Top right: support ring plate and load ring plate made of stainless steel. Bottom right: a pair of sample holders supports the specimen between two load cells in the Instron machine.

loading at a constant rate of 16.7 $\mu\text{m/s}$ until the sample breaks. The breaking load is recorded.

The fracture location and mode are inspected for each specimen. For a properly conducted equibiaxial test, fracture typically occurs on the tensile surface within the diameter of the load ring. The location of the fracture is consistently near but inside the load ring, and the origin is not always in the same place. Then the equibiaxial strength is calculated based on the breaking load, using the equation provided by the standard ASTM C1499 as

$$\sigma_f = \frac{3F}{2\pi b^2} \left((1 - \nu) \frac{D_S^2 - D_L^2}{2D^2} + (1 + \nu) \log \frac{D_S}{D_L} \right), \quad (5)$$

where F is the breaking load, b is the specimen thickness, ν is the Poisson's ratio, and D_S , D_L are diameters of the support ring and load ring, respectively. In addition, for a square plate, D is a parameter with a unit of length that can be determined from the size of the specimen.

B. Strength Test Results and Weibull Analysis

A large number of specimens have been tested and their equibiaxial strengths calculated. For simplicity, the specimens are divided into

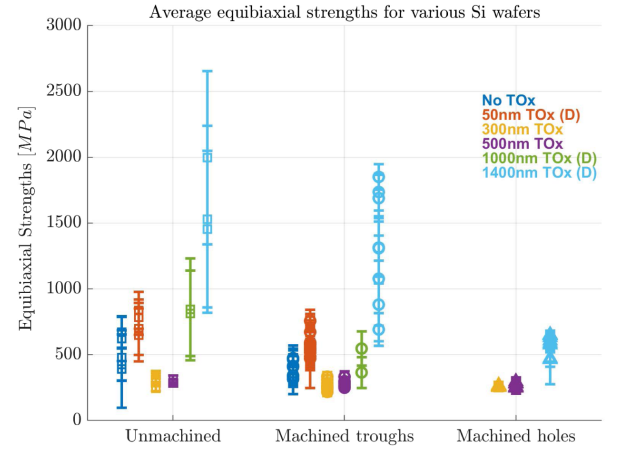


Fig. 10. Average and variance of ~ 7 tested specimens from the same silicon wafer. Wafers are grouped together based on their thermal oxides and machining situations.

three categories: unmachined, machined troughs, and machined holes. For the last two categories, there is quite a wide variety of features in each category, which affects their strength, but the difference between these different types of features within one category is much smaller than the difference between different categories. The samples are also divided according to their film thickness and the number of sides with oxide (single or double side). This distinction is important, as we will see that thermal oxide can greatly affect the strength of the materials.

In Fig. 10, we take the average of all specimens from the same silicon wafer, and plot their mean and variance according to the aforesaid categories. Each bar represents an individual wafer, and wafers belonging to the same categories are grouped together. There are six types of thermal oxide conditions, each marked by a different color. Apart from the one without any thermal oxide (which is just a bare silicon wafer), the remaining five types include three double-side thermal oxides and two single-side thermal oxides. Unmachined, machined troughs, and machined holes are represented by squares, circles, and triangles, respectively.

From the figure, we see that oxide on silicon wafers improves their strength greatly, at least in the case of double-side thermal oxide. Further, the thicker the oxide, the higher the strength. This relationship still applies even after micromachining. Laser micromachining does decrease the strength of silicon wafers in the case of double-side thermal oxide. For example, it will bring down the extremely high strength of silicon wafers with 1400 nm double-side thermal oxide by about 25% if machined with troughs. Silicon wafers with single-side thermal oxide seem to act quite differently than the cases with double-side thermal oxide or no oxide. The original value of the strength is low, and it does not seem to change much with micromachining.

To better describe the statistical behaviors in the breaking strengths of materials, we performed a Weibull analysis for each category. We fit the measured strength of all the specimens in each category using the maximum likelihood estimates (MLE) to a three-parameter Weibull distribution whose probability density function is given by

$$f(x) = \frac{\gamma}{\alpha} \left(\frac{x - \mu}{\alpha} \right)^{\gamma-1} e^{-\left(\frac{x - \mu}{\alpha} \right)^\gamma}, \quad (6)$$

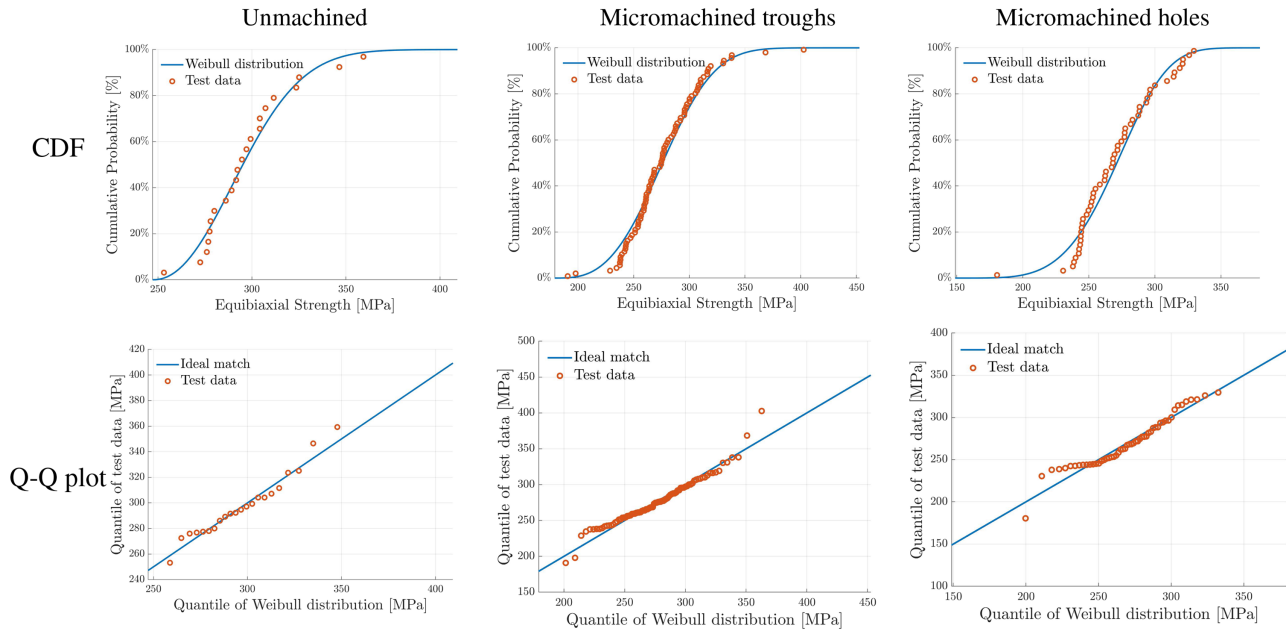


Fig. 11. Best fit Weibull distribution for wafers with 500 nm thermal oxide in all three machining categories. The first row is the CDF of the fit and empirical CDF of the data. The second row is the Q-Q plot for comparing two distributions.

where x is the breaking strength, γ is the shape parameter, α is the scale parameter (or characteristic strength), and μ is the location parameter (or threshold parameter).

We compare the empirical cumulative distribution to the cumulative density function (CDF) of the fitted distribution, to evaluate how well the fit performs. The CDF is also the unreliability function, which represents the probability of a failure occurring beyond a given strength. For example, the best fit Weibull distributions for wafers with 500 nm thermal oxide in all three machining categories are plotted in Fig. 11. The first row is the CDF of the fit and empirical CDF of the data. The second row is the quantile–quantile (Q-Q) plot for comparing two distributions. The points in the Q-Q plots approximately lie on the line $y = x$, so the two distributions being compared are similar, i.e., the fits describe the test dataset relatively well.

These Weibull parameters are then used to calculate two other reliability metrics: mean-time-to-failure (MTTF), which should be renamed in terms of strength in our work, as the expectation of the breaking strength $S_{MTTF} = \mu + \alpha \Gamma(1 + \frac{1}{\beta})$, where $\Gamma(*)$ is the gamma function; and median strength $S_{Median} = \mu + \alpha (\log 2)^{\frac{1}{\beta}}$. In general, we would like to see higher MTTF values and median strengths, which indicate that the materials are stronger. The results are summarized in Table 1.

From the above analysis, we find that for silicon wafers with single-side oxide, the side with the oxide and under compression is much stronger than the other side with bare silicon, and is unlikely to initiate a fracture (needs additional ~ 270 MPa to break). Also, the decrease in strength due to laser micromachining is small, because micromachining is applied on the surface with the oxide, yet fracture still first initiates from the bare silicon side. In other words, even after micromachining, the surface with oxide and hence under compression is still stronger than bare silicon. The bare Si wafers (with no TOx) and double-side TOx wafers have a large variance of breaking strength, which may be caused by the symmetric surface stress on both sides of the wafer surfaces. In

other words, if the top and bottom surfaces both have the same stress states (either no surface stress as in the pure Si wafer case, or comparable compressive film stress as in the double-side TOx case), the fracture may start from either surface, and breaking strengths of the specimen vary in a larger range. If only one side of the wafer surface (in this case, the top surface) has a compressive film stress, the breaking strengths of the specimen will be constrained to a much smaller range. Even though laser micromachining decreases the strength in double-side oxides by a significant amount, its resultant strength may still be higher than a bare silicon wafer without micromachining. The change of the Weibull shape parameter γ is not very obvious in micromachined troughs, but more prominent in micromachined holes. This indicates a change of flaw distribution, or the introduction of new flaw groups. Either way, this change is not necessarily a bad thing, as long as the flaws do not propagate uncontrollably (which would result in the breaking of specimen materials even before testing).

In addition, this research shows that even when not using micromachining as a stress compensation method, oxidizing the mirror to introduce a compressive thermal oxide on the surface can greatly improve the equibiaxial strength and reduce the chance of breaking. This can be applied to any Si structures flying into the sky in the future or other ceramic-type space structures, not limited to just optics or imaging devices. Static loading tests are more conservative than dynamic loading, so if the structure survives the static loading tests, it will have a higher chance to survive the dynamic loading environment (such as vibrations that occur during the launch/landing of space vehicles).

6. CONCLUSION

In summary, we demonstrated the patterning of a thermal oxide layer with two femtosecond laser systems on flat silicon mirrors. By using a simple optical setup with a scanning $x - y$ stage, we have shown that a two-dimensional stress field can be generated with laser micromachined features in a stressed thermal oxide

Table 1. Mean, Variance, and Weibull Parameters for Specimen Strengths in Each Category

Surface Conditions	# of Specimen	Average [MPa]	Standard Deviation [MPa]	Weibull parameters				
				Shape γ	Scale α [MPa]	Location μ [MPa]	MTTF [MPa]	Median [MPa]
Single-side TOx 500 nm, unmachined	22	297.5	24.8	2.2	57	247	297.2	296.1
Single-side TOx 500 nm, machined with troughs	84	277.2	33.9	3	109	179	276.7	275.9
Single-side TOx 500 nm, machined with troughs (TOx side facing down)	21	545.9	126.8	1-7	237	334	545-6	526.6
Single-side TOx 500 nm, machined with holes	53	270.2	29.7	4-5	133	149	270	271.2
Single-side TOx 300 nm, unmachined	33	302.5	47.1	2.8	130	186	302.5	300.7
Singleside TOx 300 nm, machined with troughs	86	260.9	38.9	3-2	131	143	260.6	260.1
Single-side TOx 300 nm, machined with holes	56	259.6	19.6	6.9	109	158	259.6	261.3
no TOx, unmachined	35	532.5	263.7	1.7	477	105	530.9	487.6
no TOx, machined with troughs	63	397.8	125	1.8	245	180	397.6	379.9
Double-side TOx 50 nm, unmachined	28	650.2	203.1	17	383	308	649.1	616.9
Double-side TOx 50 nm, machined with troughs	105	571.7	188.6	2.4	487	138	569.9	556.9
Double-side TOx 1000 nm, unmachined	14	829.6	342.9	14	559	317	825.5	745.9
Double-side TOx 1000 nm, machined with troughs	14	455.8	151.5	2-3	363	132	453.3	437.9
Double-side TOx 1400 nm, unmachined	19	1673.8	662.9	2	1519	295	1647.5	1574.6
Double-side TOx 1400 nm, machined with troughs	54	1290.7	515.2	1.9	1098	305	1279.5	1209
Double-side TOx 1400 nm, machined with holes	66	590.7	102.2	4-9	420	202	589.2	594.6

film, which can be used to induce controlled bending in thin silicon mirrors for correcting its figure errors and compensating for coating distortions. A stress field can be generated through the selective removal of stressed film regions and attached substrate regions. To be more specific, we showed that patterned removal of uniformly distributed holes leads to equibiaxial stress states, while fine-pitched oriented removal of periodic troughs generates non-equibiaxial stress components. The combination of these two features, with proper rotation of trough orientation, can create a variety of stress states that can be used to correct for many different error terms in the mirrors. We also demonstrated the multi-pass correction capability of this approach for inducing controlled deformations in thin mirrors [38]. Additionally, we performed a series of tests to evaluate the strength of the thin mirrors after being treated with ultrafast laser micromachining. For silicon mirrors with single-side thermal oxide, the decrease in strength of mirror materials (Si wafer with SiO₂ film) due to laser micromachining is small. For silicon mirrors with double-side thermal oxide, the introduction of micromachined features decreased the strength (by ~25% with troughs), while the resultant strengths are still higher than bare Si wafers without micromachining. Therefore, this technology could be a viable method for processing materials and optics for space applications.

In short, the femtosecond laser micromachining technique provides a fast, simple, and straightforward way to correct mirror figure errors by writing patterns on the back surface of the mirror substrates with ultrafast lasers. Our experiments and tests show that it can be a possible candidate for trimming stress for thin space optics

in the stress compensation step, and it does not greatly compromise strength if applied properly.

Funding. National Aeronautics and Space Administration (80NSSC20K0907).

Acknowledgment. The authors thank Dr. Brandon Chalifoux and Dr. Kyung-han Hong for many meaningful and interesting discussions, and thank AOptoWave Inc. for providing the femtosecond lasers used in the experiments. We also thank MIT facilities (MRSEC, DMSE) for providing the instruments and test machines.

Disclosures. The authors declare no conflicts of interest.

Data availability. Data underlying the results presented in this paper are not publicly available at this time but may be obtained from the authors upon reasonable request.

REFERENCES

1. J. A. Gaskin, D. Swartz, A. A. Vikhlinin, *et al.*, "Lynx X-ray Observatory: an overview," *J. Astron. Telesc. Instrum. Syst.* **5**, 021001 (2019).
2. K. Patterson and S. Pellegrino, "Ultralightweight deformable mirrors," *Appl. Opt.* **52**, 5327–5341 (2013).
3. W. W. Zhang, K. D. Allgood, M. Biskach, K.-W. Chan, M. Hlinka, J. D. Kearney, J. R. Mazzarella, R. S. McClelland, A. Numata, and R. E. Riveros, "High-resolution, lightweight, and low-cost x-ray optics for the Lynx Observatory," *J. Astron. Telesc. Instrum. Syst.* **5**, 021012 (2019).
4. M. J. Collon, G. Vacanti, N. M. Barrière, *et al.*, "Silicon pore optics mirror module production and testing," *Proc. SPIE* **11180**, 1118023 (2019).
5. W. W. Zhang, K. D. Allgood, M. P. Biskach, K.-W. Chan, M. Hlinka, J. D. Kearney, J. R. Mazzarella, R. S. McClelland, A. Numata, L. G. Olsen, R. E. Riveros, T. T. Saha, and P. M. Solly, "Monocrystalline silicon and the

- meta-shell approach to building x-ray astronomical optics," *Proc. SPIE* **10399**, 103990S (2017).
6. R. E. Riveros, M. P. Biskach, K. D. Allgood, J. D. Kearney, M. Hlinka, A. Numata, and W. W. Zhang, "Fabrication of lightweight silicon x-ray mirrors for high-resolution x-ray optics," *Proc. SPIE* **10699**, 106990P (2018).
 7. K.-W. Chan, M. Sharpe, W. Zhang, L. Kolos, M. Hong, R. McClelland, B. Hohl, T. Saha, and J. Mazzarella, "Coating thin mirror segments for lightweight x-ray optics," *Proc. SPIE* **8861**, 88610X (2013).
 8. D. M. Broadway, J. Weimer, D. Gurgew, T. Lis, B. D. Ramsey, S. L. O'Dell, M. Gubarev, A. Ames, and R. Bruni, "Achieving zero stress in iridium, chromium, and nickel thin films," *Proc. SPIE* **9510**, 95100E (2015).
 9. H. Mori, T. Okajima, W. W. Zhang, K.-W. Chan, R. Koenecke, J. R. Mazzarella, A. Numata, L. G. Olsen, R. E. Riveros, and M. Yukita, "Reflective coatings for the future x-ray mirror substrates," *Proc. SPIE* **10699**, 106994I (2018).
 10. F. E. Christensen, A. C. Jakobsen, N. F. Brøjnholt, K. K. Madsen, A. Hornstrup, N. J. Westergaard, J. Momberg, J. Koglin, A. M. Fabricant, M. Stern, W. W. Craig, M. J. Pivovarov, and D. Windt, "Coatings for the NuSTAR mission," *Proc. SPIE* **8147**, 81470U (2011).
 11. D. D. M. Ferreira, S. Svendsen, S. Massahi, A. Jafari, L. M. Vu, J. Korman, N. C. Gellert, F. E. Christensen, S. Kadkhodazadeh, T. Kasama, B. Shortt, M. Bavdaz, M. J. Collon, B. Landgraf, M. Krumrey, L. Cibik, S. Schreiber, and A. Schubert, "Performance and stability of mirror coatings for the ATHENA mission," *Proc. SPIE* **10699**, 106993K (2018).
 12. B. D. Chalifoux, Y. Yao, R. K. Heilmann, and M. L. Schattenburg, "Simulations of film stress effects on mirror segments for the Lynx X-ray Observatory concept," *J. Astron. Telesc. Instrum. Syst.* **5**, 021004 (2019).
 13. S. Kohli, C. D. Rithner, and P. K. Dorhout, "X-ray characterization of annealed iridium films," *J. Appl. Phys.* **91**, 1149–1154 (2002).
 14. Z. Jiang, X. Jiang, W. Liu, and Z. Wu, "Thermal stability of multilayer films Pt/Si, W/Si, Mo/Si, and W/C," *J. Appl. Phys.* **65**, 196–200 (1989).
 15. M. Ghigo, G. Vecchi, S. Basso, O. Citterio, M. Civitani, E. Mattaini, G. Pareschi, and G. Sironi, "Ion figuring of large prototype mirror segments for the E-ELT," *Proc. SPIE* **9151**, 91510Q (2014).
 16. S. Trolier-McKinstry and P. Muralt, "Thin film piezoelectrics for MEMS," *J. Electroceram.* **12**, 7–17 (2004).
 17. J. Walker, T. Liu, M. Tendulkar, D. N. Burrows, C. T. DeRoo, R. Allured, E. N. Hertz, V. Cotroneo, P. B. Reid, E. D. Schwartz, T. N. Jackson, and S. Trolier-McKinstry, "Design and fabrication of prototype piezoelectric adjustable x-ray mirrors," *Opt. Express* **26**, 27757–27772 (2018).
 18. C. T. DeRoo, R. Allured, V. Cotroneo, E. N. Hertz, V. Marquez, P. B. Reid, E. D. Schwartz, Sr., A. A. Vikhlinin, S. Trolier-McKinstry, J. Walker, T. N. Jackson, T. Liu, and M. Tendulkar, "Deterministic figure correction of piezoelectrically adjustable slumped glass optics," *J. Astron. Telesc. Instrum. Syst.* **4**, 019004 (2018).
 19. B. Chalifoux, Y. Yao, H. E. Zuo, R. K. Heilmann, and M. L. Schattenburg, "Compensating film stress in silicon substrates for the Lynx X-ray Telescope Mission concept using ion implantation," *Proc. SPIE* **10699**, 1069959 (2018).
 20. B. D. Chalifoux, Y. Yao, K. B. Woller, R. K. Heilmann, and M. L. Schattenburg, "Compensating film stress in thin silicon substrates using ion implantation," *Opt. Express* **27**, 11182–11195 (2019).
 21. Y. Yao, B. D. Chalifoux, R. K. Heilmann, and M. L. Schattenburg, "Thermal oxide patterning method for compensating coating stress in silicon substrates," *Opt. Express* **27**, 1010–1024 (2019).
 22. B. N. Chichkov, C. Momma, S. Nolte, F. Von Alvensleben, and A. Tünnermann, "Femtosecond, picosecond and nanosecond laser ablation of solids," *Appl. Phys. A* **63**, 109–115 (1996).
 23. S. Sundaram and E. Mazur, "Inducing and probing non-thermal transitions in semiconductors using femtosecond laser pulses," *Nat. Mater.* **1**, 217 (2002).
 24. S. Nolte, M. Will, J. Burghoff, and A. Tünnermann, "Femtosecond waveguide writing: a new avenue to three-dimensional integrated optics," *Appl. Phys. A* **77**, 109–111 (2003).
 25. R. R. Gattass and E. Mazur, "Femtosecond laser micromachining in transparent materials," *Nat. Photonics* **2**, 219–225 (2008).
 26. B. D. Chalifoux, R. K. Heilmann, and M. L. Schattenburg, "Correcting flat mirrors with surface stress: analytical stress fields," *J. Opt. Soc. Am. A* **35**, 1705–1716 (2018).
 27. L. B. Freund and S. Suresh, *Thin Film Materials: Stress, Defect Formation and Surface Evolution* (Cambridge University, 2004).
 28. A. Wikström, P. Gudmundson, and S. Suresh, "Thermoelastic analysis of periodic thin lines deposited on a substrate," *J. Mech. Phys. Solids* **47**, 1113–1130 (1999).
 29. Y.-L. Shen, S. Suresh, and I. Blech, "Stresses, curvatures, and shape changes arising from patterned lines on silicon wafers," *J. Appl. Phys.* **80**, 1388–1398 (1996).
 30. H. E. Zuo, B. D. Chalifoux, R. K. Heilmann, and M. L. Schattenburg, "Ultrafast laser micro-stressing for correction of thin fused silica optics for the Lynx X-ray Telescope Mission," *Proc. SPIE* **10699**, 1069954 (2018).
 31. E. Kobeda and E. Irene, "Intrinsic SiO₂ film stress measurements on thermally oxidized Si," *J. Vac. Sci. Technol. B* **5**, 15–19 (1987).
 32. J. Fitch, C. Bjorkman, G. Lucovsky, F. Pollak, and X. Yin, "Intrinsic stress and stress gradients at the SiO₂/Si interface in structures prepared by thermal oxidation of Si and subjected to rapid thermal annealing," *J. Vac. Sci. Technol. B* **7**, 775–781 (1989).
 33. G. G. Stoney, "The tension of metallic films deposited by electrolysis," *Proc. R. Soc. London A* **82**, 172–175 (1909).
 34. E. S. Claflin and N. Bareket, "Configuring an electrostatic membrane mirror by least-squares fitting with analytically derived influence functions," *J. Opt. Soc. Am. A* **3**, 1833–1839 (1986).
 35. D. Ngo, Y. Huang, A. Rosakis, and X. Feng, "Spatially non-uniform, isotropic misfit strain in thin films bonded on plate substrates: The relation between non-uniform film stresses and system curvatures," *Thin Solid Films* **515**, 2220–2229 (2006).
 36. Y. Huang, D. Ngo, X. Feng, and A. Rosakis, "Anisotropic, non-uniform misfit strain in a thin film bonded on a plate substrate," *Interact. Multiscale Mech.* **1**, 123–142 (2007).
 37. Y. Yao, B. Chalifoux, R. Heilmann, and M. Schattenburg, "Stress tensor mesostructures for freeform shaping of thin substrates," arXiv:2108.00575 (2021).
 38. H. E. Zuo, B. D. Chalifoux, R. K. Heilmann, S.-H. Nam, K.-H. Hong, and M. L. Schattenburg, "Demonstration of femtosecond laser micromachining for figure correction of thin silicon optics for x-ray telescopes," *Proc. SPIE* **11119**, 111191A (2019).
 39. T. Crawford, J. Yamanaka, G. Botton, and H. Haugen, "High-resolution observations of an amorphous layer and subsurface damage formed by femtosecond laser irradiation of silicon," *J. Appl. Phys.* **103**, 053104 (2008).
 40. H. E. Zuo, R. Heilmann, and M. Schattenburg, are preparing a manuscript to be called "Analysis of stresses and shape changes in thin optics with stressed film patterning using femtosecond laser micromachining."
 41. H. E. Zuo, "Ultrafast laser micromachining for correction of thin optics for next generation x-ray space telescopes," Ph.D. thesis (Massachusetts Institute of Technology, 2021).